

Enabling Low-Latency Machine learning on Radiation-Hard FPGAs with hls4ml

Katya Govorkova 

Massachusetts Institute of Technology (MIT), 77 Massachusetts Ave,
Cambridge, MA 02139, USA

E-mail: ekaterina.govorkova@cern.ch

Julián García Pardiñas 

Massachusetts Institute of Technology (MIT), 77 Massachusetts Ave,
Cambridge, MA 02139, USA

E-mail: julian.garcia.pardinias@cern.ch

Vladimir Lončar 

Department of Experimental Physics, European Organization for
Nuclear Research (CERN), 1211 Geneva 23, Switzerland

E-mail: vladimir.loncar@cern.ch

Victoria Nguyen 

Massachusetts Institute of Technology (MIT), 77 Massachusetts Ave,
Cambridge, MA 02139, USA

E-mail: vkn@mit.edu

Sebastian Schmitt 

Massachusetts Institute of Technology (MIT), 77 Massachusetts Ave,
Cambridge, MA 02139, USA

E-mail: s.schmitt@cern.ch

Marco Pizzicemi 

University of Milano-Bicocca (Italy), and
Department of Experimental Physics, European Organization for
Nuclear Research (CERN), 1211 Geneva 23, Switzerland

Loris Martinazzoli 

Department of Experimental Physics, European Organization for
Nuclear Research (CERN), 1211 Geneva 23, Switzerland

E-mail: loris.martinazzoli@cern.ch

Eluned Anne Smith 

Massachusetts Institute of Technology (MIT), 77 Massachusetts Ave,
Cambridge, MA 02139, USA

E-mail: eluned@mit.edu

Abstract.

This paper presents the first demonstration of a viable, ultra-fast, radiation-hard machine learning (ML) application on FPGAs, which could be used in future high-energy physics experiments. We present a three-fold contribution, with the PicoCal calorimeter, planned for the LHCb Upgrade II experiment, used as a test case. First, we develop a lightweight autoencoder to compress a 32-sample timing readout, representative of that of the PicoCal, into a two-dimensional latent space. Second, we introduce a systematic, hardware-aware quantization strategy and show that the model can be reduced to 10-bit weights with minimal performance loss. Third, as a barrier to the adoption of on-detector ML is the lack of support for radiation-hard FPGAs in the High-Energy Physics community’s standard ML synthesis tool, `hls4ml`, we develop a new backend for this library. This new back-end enables the automatic translation of ML models into High-Level Synthesis (HLS) projects for the Microchip PolarFire family of FPGAs, one of the few commercially available and radiation hard FPGAs. We present the synthesis of the autoencoder on a target PolarFire FPGA, which indicates that a latency of 25 ns can be achieved. We show that the resources utilized are low enough that the model can be placed within the inherently protected logic of the FPGA. Our extension to `hls4ml` is a significant contribution, paving the way for broader adoption of ML on FPGAs in high-radiation environments.

Keywords: Machine Learning, FPGA, Radiation Hardness, High-Energy Physics, `hls4ml`, LHCb, PolarFire, SmartHLS, Autoencoder, Data Compression

1. Introduction

The pursuit of new physics at the frontiers of energy and intensity requires constant innovation in detector technology and real-time data processing. The upcoming High-Luminosity Large Hadron Collider (HL-LHC) era is set to deliver an unprecedented volume of data [1]. This increase in discovery potential is accompanied by formidable challenges, most notably a massive increase in data rates and a higher number of simultaneous proton-proton collisions (pile-up). To handle this growing volume of data, experiments are increasingly forced to deploy powerful computational solutions as close to the detectors as possible. This “edge computing” strategy minimizes data transmission latency and bandwidth but necessitates that compression be performed on electronics in harsh radiation environments [2]. Consequently, there is a pressing need for ultra-fast, low-latency, and radiation-hard machine learning (ML) applications that can intelligently filter and compress data at the extreme edge of the readout chain.

The Large Hadron Collider beauty (LHCb) experiment’s Upgrade II, planned to take place during the fourth Long Shutdown of the LHC, provides a compelling and concrete example of this challenge [3]. This upgrade is designed to operate at a

significantly higher instantaneous luminosity than before of up to $1.5 \times 10^{34} \text{ cm}^{-2} \text{ s}^{-1}$, which will increase the average pile-up to approximately 40. This higher collision rate, combined with the inherently large production cross-sections for the beauty and charm hadrons that LHCb targets, will generate an unprecedented data rate of 200 Tb/s, a volume that necessitates significant detector enhancements. An example of such a detector enhancement is the planned, high-granularity electromagnetic calorimeter with excellent timing capabilities, known as the PicoCal [4]. To achieve its target time resolution of 10 – 20 ps, the SPIDER [5], a waveform digitizer ASIC, will digitize the pulse shape from each calorimeter read-out channel. This pulse shape represents the time evolution of the voltage induced by the cascade of electrons produced within a photomultiplier tube (PMTs) [4] in response to scintillation photons generated by an electromagnetic shower in the calorimeter. While the final number of samples is yet to be determined, with current estimates ranging from 8 to 32, this study assumes the pulse shape is represented by 32 16-bit numbers. The sampling interval is chosen such that the pulse rise time, defined as the time between the points where the pulse reaches 10% and 90% of its maximum amplitude, is captured by approximately four to five sampling points. This granularity is assumed to very roughly represent that expected of the LHCb PicoCal readout. However, it should be stressed that the performance of the machine-learning-based compression algorithms, which is the focus of this paper, should not depend critically on the precise granularity of the readout. It is estimated that in order to have tenable data-rates between the on-detector front-end electronics and the backend electronics, the initial sample of 32 inputs must be compressed into a maximum of two numbers of a similar bit size on the detector. This work aims to achieve this compression ratio whilst still maintaining as much information about the pulse as possible. The hardware platform chosen for this design study is the Microchip PolarFire FPGA, a device selected for its inherent radiation tolerance. The technical motivations for this choice, which relate to its flash-based architecture as a superior alternative to traditional SRAM-based FPGAs requiring Triple Modular Redundancy (TMR), are detailed in Section 2.3.

In high-energy physics, a common alternative to FPGAs is a custom Application-Specific Integrated Circuit (ASIC). However, the inflexible, multi-year development cycle and high non-recurring engineering costs mean ASICs are typically only used when extreme performance or power constraints cannot be met by programmable hardware. This work also serves to demonstrate that FPGAs can represent a viable alternative to ASICs for ML algorithms that must satisfy both demanding real-time requirements and run on-detector, in high-radiation environments.

At the outset of this work, two key components for tackling the PicoCal data compression challenge were missing. First, no specific ML algorithm had been developed and validated for compression of the full pulse shape. Second, the high-level synthesis for machine learning (`hls4ml`) toolchain, a community standard for deploying ML models on FPGAs, lacked support for radiation-hard Microchip devices [6]. This paper addresses these gaps with a three-fold contribution:

- (i) **An ML Algorithm for Pulse Compression:** We develop and validate a lightweight autoencoder model designed specifically for the LHCb PicoCal use case. We demonstrate through simulation that this model can effectively compress the 32-sample pulse shapes into a compact two-dimensional latent space, preserving the information required for downstream physics reconstruction.
- (ii) **Hardware-Aware Model Compression:** We conduct a systematic study of model quantization, demonstrating a methodology to drastically reduce the model’s computational complexity while preserving physics reconstruction performance.
- (iii) **A New Backend for `hls4ml`:** We develop a new software backend for the `hls4ml` library to support the Microchip SmartHLS compiler ‡ [7]. This critical infrastructure work enables, for the first time, the automated deployment of ML models onto radiation-hard Polar Fire FPGAs, opening the door for the wider high-energy physics community to leverage these devices for on-detector ML applications.

The result is the first end-to-end demonstration of a viable, ultra-fast ML application on a radiation-hard FPGA for a future high-energy physics experiment, a milestone enabled by the new automated design flow also developed as part of this work.

For this design study, key performance and architectural parameters were established based on preliminary discussions with experts involved in the LHCb Upgrade II electronics design. A baseline scenario assumes that each front-end FPGA will need to process data from 8 independent calorimeter channels in parallel. Furthermore, while the LHC bunch crossing rate is 40 MHz, a target for the FPGA’s internal processing clock of 160 MHz is considered a realistic benchmark. This choice allows for exactly four internal clock cycles to process each new input, setting a strict latency and throughput requirement for the compression algorithm.

This paper is structured as follows. We first review related work in ML-based data compression and FPGA deployment toolchains in Section 2. In Section 3, we describe the architecture of our autoencoder model and demonstrate its ability to compress and faithfully reconstruct pulse shapes while preserving key physics information. Section 4 details the hardware-aware quantization study performed to optimize the model for hardware implementation. In Section 5, we present the development of the new `hls4ml` backend and the final synthesis results on the target PolarFire FPGA, showing that the design meets the application’s strict performance requirements. Finally, we discuss the broader implications of these results in Section 6 and present our conclusions in Section 7.

2. Related Work

This work builds upon established techniques in two distinct domains: the use of autoencoders for data processing in high-energy physics and the deployment of machine

‡ Microchip SmartHLS Tool Suite, Version 2021.2, Microchip Technology Inc., Chandler, AZ, USA.

learning models on FPGAs using high-level synthesis tools. This section reviews the state-of-the-art in both areas to contextualize our contributions.

2.1. Data Compression and Anomaly Detection with Autoencoders

The immense data volume at the LHC has driven the widespread exploration of machine learning for real-time data reduction and analysis [8]. Autoencoders, as a class of unsupervised neural networks, have proven to be particularly effective. They are trained to learn a compressed, low-dimensional representation (latent space) of high-dimensional data by reconstructing their own input, forcing the model to capture the most salient features of the data distribution.

In high-energy physics, this technique has been successfully applied to a range of problems. These include the compression of jet substructure information for trigger systems and offline storage, as well as model-agnostic anomaly detection, where events that are poorly reconstructed from the latent space are flagged as potential new physics [9]. Other studies have explored the physical meaning of the latent space itself, demonstrating that its learned variables can be correlated with underlying physical processes, forming a powerful feature space for analysis [10]. Our work applies this paradigm to a novel and challenging use case: the on-detector, ultra-low-latency compression of full calorimeter pulse shapes, where preserving timing information is critical and preserving other pulse-shape information, such as the rise-time, is desirable.

2.2. ML-to-FPGA Toolchains and Radiation-Hard Hardware

For ML models to be deployed at the detector front-end, they must meet stringent real-time processing constraints, with latencies typically ranging from nanoseconds to a few microseconds [6]. FPGAs are an ideal hardware platform for this task, enabling massively parallel and deeply pipelined implementations that eliminate external memory bottlenecks. The high-energy physics community has largely standardized on the `hls4ml` library for translating ML models from frameworks like TensorFlow/Keras into FPGA firmware. It has been successfully used to deploy a variety of models, from dense neural networks to recurrent networks, with latencies on the order of hundreds of nanoseconds. While commercial toolchains like Xilinx Vitis AI and Intel OpenVINO offer powerful solutions for deploying ML models on FPGAs, they are often tailored to specific vendor architectures and target a more general processing style with data and model residing in off-chip memory. In contrast, `hls4ml` real-time processing with models deployed fully on-chip is particularly well-suited to the needs of the scientific community, enabling fine-grained control over the hardware implementation and facilitating the integration of new backends, as demonstrated in this work. Furthermore, such automated workflows are crucial for enabling rapid design space exploration, such as systematically varying model quantization, which would be significantly time-consuming with a purely manual HLS implementation.

However, `hls4ml` has historically supported HLS compilers exclusively for commercial FPGAs from Xilinx (now AMD) and Intel, which are typically SRAM-based. At the outset of this project, the lack of a streamlined, high-level toolchain for deploying ML models onto the radiation-hard, flash-based Microchip devices considered for this work was a primary barrier to their adoption. This work closes that gap by developing and validating the first `hls4ml` backend for this class of FPGAs, providing an automated and open-source path from a high-level ML model to a hardware implementation on a radiation-hard platform.

2.3. Radiation Hardness Paradigms in FPGAs

Deploying electronics in the LHC’s radiation environment necessitates robust mitigation against Single Event Effects (SEEs), which can disrupt circuit operation. For FPGAs, the mitigation strategy is intrinsically linked to the underlying technology of the configuration memory.

SRAM-based FPGAs, the most common commercial option, store their logic configuration in static RAM cells susceptible to SEUs, where a charged particle can corrupt the device’s logic function. The standard mitigation technique is Triple Modular Redundancy (TMR), where logic is triplicated and a voter system corrects any single fault [11]. While effective, TMR imposes a significant overhead of at least 3x in logic resources, increased power consumption, and considerable design complexity.

In contrast, flash-based FPGAs, such as the Microchip PolarFire family used in this work, offer an alternative paradigm. Their configuration is stored in non-volatile flash memory cells, which are inherently immune to these configuration SEUs. This “radiation-hardened-by-design” approach avoids the need for configuration TMR, offering a path to reliable systems with significantly lower complexity and resource utilization. This fundamental difference was a key motivator for the hardware choice in this design study. The interplay between algorithm design, mitigation techniques, and the inherent robustness of the hardware is explored further in Section 6.

3. Autoencoder Architecture and Co-Design Rationale

We aim to develop a lightweight autoencoder that achieves a high compression ratio while preserving the full pulse-shape information. Although extracting a single timestamp from the pulse shape is the most critical piece of information, retaining the full shape is highly desirable, as it provides additional insight into shower formation in the calorimeter and can help further mitigate pile-up effects. The following subsections detail the autoencoder’s specific architecture, its training, and its performance against key physics metrics. The algorithm performance presented in this section corresponds to results obtained after quantization-aware training, which motivated the choice to represent the latent space using two 10-bit values. The procedure used to implement and optimize this quantization-aware training is described in Section 4.

3.1. Model Architecture and Co-Design Rationale

The autoencoder's architecture was co-designed with its hardware implementation in mind, prioritizing a minimal footprint and the lowest possible latency. The hardware-implemented portion is the encoder, which performs the on-detector data compression. It consists of two sequential layers:

- A fully-connected dense layer that maps the 32 input data points directly to the two-dimensional latent space.
- A Rectified Linear Unit (ReLU) activation function is applied to the two latent space variables.

This involved directing the HLS compiler to create a highly parallel, pipelined architecture, relying on partially or fully unrolled loops, avoiding any resource sharing that would increase the processing time. This ensures that an inference can be completed in the minimum number of clock cycles, a critical requirement for the front-end application.

For completeness, the decoder half of the autoencoder, used during training to reconstruct the pulse shape from the latent space, is constructed as a mirror of the encoder. It consists of a single fully-connected dense layer that maps the two latent space variables back to the 32-dimensional space of the output pulse shape. A linear activation function is used for this final layer to allow the output values to span the full, unconstrained range of the digitized pulse samples.

3.2. Simulation Dataset

The dataset used for training and evaluation consists of pulse shapes generated from a dedicated Monte Carlo simulation of the LHCb PicoCal electromagnetic calorimeter prototype [12], implemented using the Geant4 toolkit [13]. The simulation accurately models the detector geometry, material properties, and readout electronics to reproduce realistic signal responses under expected Run 5 conditions.

Two types of samples were prepared and then merged to mimic realistic detector conditions. Signal pulses correspond to the responses of SpaCal modules with a Pb absorber [12] to a single photon generated with energies uniformly distributed between $0.5 < E_T < 5$ GeV, close to the proton-proton interaction point. Those are merged with background pulses, which were generated separately to represent pile-up and underlying event conditions. These were simulated assuming a fixed luminosity of $1.5 \times 10^{34} \text{ cm}^{-2} \text{ s}^{-1}$ [12]. After generation, signal and background pulses were combined to emulate the complex conditions expected in LHCb Run 5 data-taking.

Each pulse was simulated with 1024 consecutive data points, reflecting the output of the DRS4-based V1742 CAEN digitizer (5 Gs/s, 500 MHz bandwidth) [14] used in the test beam setup. In the actual calorimeter, however, a different digitizer will be employed, providing only 32 samples per pulse. To match this configuration, we downsample the simulated waveforms from 1024 to 32 data points, with the rise-time

of a typical pulse shape represented by around 1-3 sampling intervals. This is achieved by taking every 9 samples starting at the 380th to 668 out of 1024.

3.3. Training

We implemented fully connected autoencoders to reconstruct calorimeter pulse shapes represented as 32-sample vectors. The implementation was carried out using TensorFlow [15] with the Keras high-level API [16]. We train a full precision model as well as a quantized model for the FPGA implementation. The details about the quantization are covered in Section 4.

Training was performed using the Adam optimizer with a learning rate of 10^{-3} and the Mean Squared Error (MSE) loss function. Models were trained for up to 20 epochs with an early stopping criterion (patience of 5 epochs) based on validation loss to prevent overfitting. A batch size of 32 was applied during all experiments. The dataset of 353513 calorimeter pulses was split into 70% training, 15% validation, and 15% test sets using a fixed random seed to ensure reproducibility. We used the "keras_tuner" [16] random search to select the best learning rate and best model architecture by minimizing the MSE loss together with the number of FLOPS (number of floating point operations per second). Since our input size was 32, we searched over the space of 15 combinations of keeping/dropping layers corresponding to sizes of 16, 8, 4, and 2 while maintaining that we always had at least one layer in the middle. We converged on a 32-2 structure, as the MSE loss was approximately the same, and this was the smallest model with the smallest number of flops. Before tuning the architecture, we tested using different activation functions (relu, elu, tanh), from which the relu activation function was found to be most performant. We additionally tested using different loss functions (Mean Squared Error, Mean Absolute Error, Huber, and Logcosh), but found no difference in performance.

The training process was monitored using both training and validation loss, as shown in Figure 1. The fact that the validation loss falls below the training loss is purely a statistical fluctuation, determined by the random seed used in partitioning the training and validation datasets. The best-performing weights, determined by the minimum validation loss, were restored at the end of training. After training, models were evaluated on the held-out test set using the MSE metric.

3.4. Pulse Shape Reconstruction Performance

The performance of the trained autoencoder was initially assessed by visually comparing original input pulse shapes with their reconstructed counterparts and by evaluating the MSE on the test set. Figure 2 presents several representative examples where the original waveforms (solid lines) are overlaid with reconstructions (dashed lines) obtained after compression into the 2-dimensional latent space. The green line shows the reconstruction using 32-bit precision for the latent space variables, and the pink line using 10-bit precision, as discussed in Sec. 4.

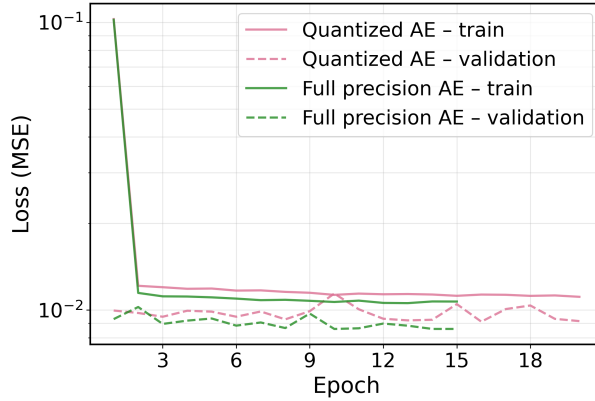


Figure 1. Training and validation loss curves for the full-precision autoencoder (in green) and the quantized autoencoder (in pink), discussed fully in Sec. 4. The y-axis uses a logarithmic scale to emphasize convergence behavior.

The close visual alignment between the original and reconstructed signals across a wide range of amplitudes confirms that the autoencoder effectively preserves both global and fine-grained features of the calorimeter response. This observation is consistent with the low average MSE values measured on the validation and test sets, demonstrating that the model achieves high-fidelity reconstruction even for challenging cases such as pulses with significant noise or extended tails.

3.5. Latent Space Analysis

To assess the interpretability of the learned latent space, we analyzed its correlation with key physical properties of the pulse shapes: *true timestamp* (time of arrival of the simulated particle to the PicoCal), *peak amplitude* and *rising time*, where the latter provides a shape-sensitive indicator of the signal development.

Figure 3 summarizes the Pearson and Spearman correlation coefficients between the two latent variables (z_0, z_1) and these physical quantities.

The results reveal a clear structure in the latent space. The second dimension (z_1) shows an almost perfect positive correlation with the *peak amplitude* (Pearson = 0.979, Spearman = 0.977), indicating that this axis primarily encodes amplitude-related information. The first latent variable (z_0) also correlates with amplitude (Pearson = 0.925), suggesting it captures secondary shape-dependent features.

Both latent variables exhibit modest negative correlations with the *true timestamp* (Pearson ≈ -0.11 to -0.16) and the *rising time* (Pearson up to -0.17), with stronger monotonic relationships indicated by the Spearman coefficients for z_0 (-0.703) and z_1 (-0.012). This suggests that timing and shape information are partially disentangled in the latent representation, although less strongly than amplitude.

Overall, these findings indicate that the autoencoder does not operate as a “black box” but rather organizes the two-dimensional latent space with one dimension dominated by amplitude information, and another influenced by shape and timing

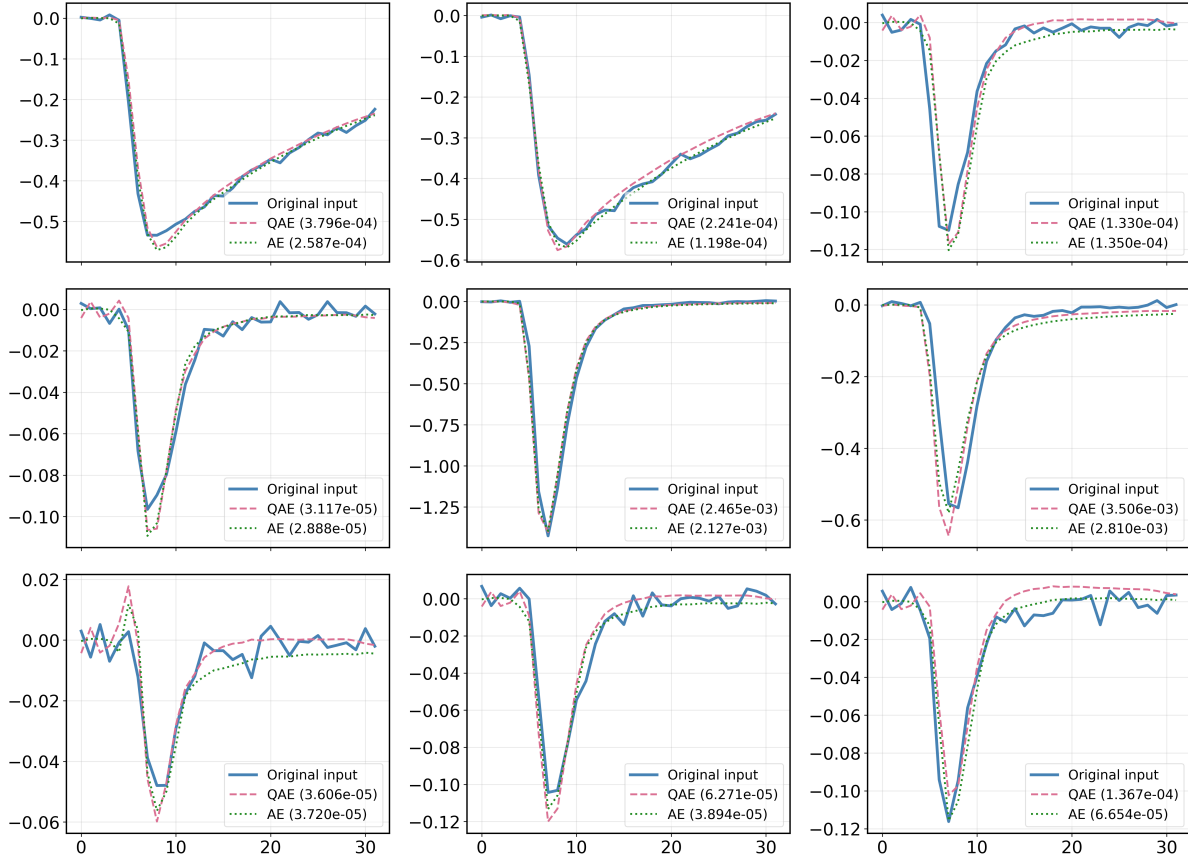


Figure 2. Examples of autoencoder reconstruction performance on calorimeter pulse shapes from the test set. Original waveforms (solid blue lines) are compared with their corresponding reconstructions (dashed lines). In green is the full precision model, and in pink is the quantized model, discussed in Sec. 4. Visual agreement is supported by low MSE values across diverse pulse amplitudes, highlighting the robustness of the reconstruction.

variations. This interpretable structure increases confidence that the compression preserves the essential physics characteristics necessary for downstream tasks such as time reconstruction.

3.6. Validation of Timestamp and Rise-time Reconstruction

Time reconstruction, expressed as a timestamp, refers to determining the precise arrival time of a signal from the pulse shape it generates in the PMT. This is typically done using algorithms such as the Constant Fraction Discrimination (CFD) [17]. Preserving this information after compression is crucial, as it underpins the ability to correctly group cells originating from the same incoming particle in the high pile-up environment of LHCb Upgrade II, and to associate the particle with the correct proton–proton interaction [12].

As further validation of our autoencoder, we therefore wish to apply the standard CFD timing algorithm to both the original and the autoencoder-reconstructed pulses

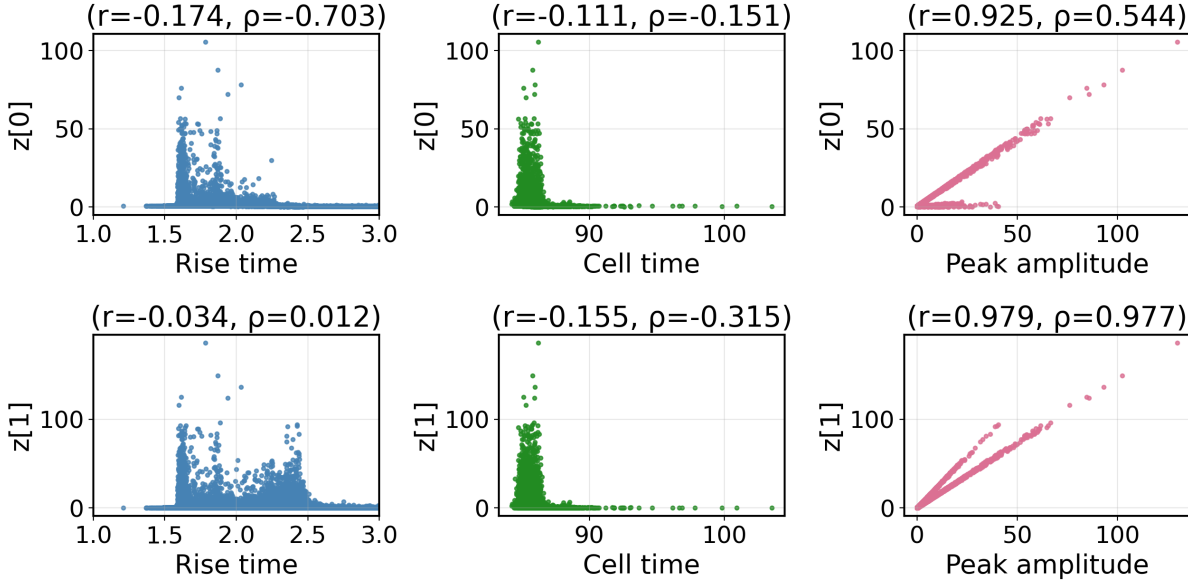


Figure 3. Correlation between latent space variables of the full-precision autoencoder and three pulse-level features on the test set: rise time (10%–90% interval), pulse true timestamp, and peak amplitude. Each row corresponds to one latent dimension ($z[0]$, $z[1]$), and each column to one feature. Scatter plots include Pearson’s r and Spearman’s ρ coefficients in the titles. The latent representation is strongly correlated with peak amplitude, while correlations with timing features (rise time and cell time) are weaker.

from the held-out test set, and compare both with the true timestamp.

While injecting the underlying event into the baseline simulation produces a more realistic readout scenario, it obscures the true arrival time of a pulse, because it is no longer possible to determine whether a given pulse shape originates from an injected signal photon (for which the true time is known) or from other photons in the event (for which it is not). As a result, the timestamp reconstruction is tested on pulses from so-called seed cells only. To identify these, we perform a simple clustering of cells, selecting the one with the highest local energy (the seed cell). We then match clusters to the true simulated photons. Taking the seed cell from the matched cluster ensures that the arrival time corresponds to the simulated photon and not to the underlying event; therefore, we can use it to perform the time-extraction study detailed below. Additionally, two distinct types of pulses are observed due to the geometry of the spaghetti calorimeter (SpaCal), which is the detector type in the central region of the PicoCal [12], composed of longitudinal scintillators intersected by a mirror along the longitudinal plane. Photons can either be reflected by this mirror and read out at the front of the SpaCal (front pulses) or they can originate beyond the mirror and be read out at the back of the SpaCal (back pulses). These two pulse-types have different offsets from the true arrival time, due to differing distances between the active material and the read-out, and so for the purpose of validation, we restrict the data-set to just one pulse-type (front pulses). It should be stressed, however, that it is still the baseline autoencoder used in the

validation, i.e. trained on both pulse-types and quantized to 10 bits.

The CFD algorithm estimates the signal timestamp by finding the point at which the pulse crosses a fixed fraction (20%) of its maximum amplitude after baseline subtraction. The same CFD configuration was adopted for both original and autoencoder-reconstructed pulses to ensure a fair comparison. The reconstructed timestamps were then compared against the ground-truth timing, corresponding to the simulated time of arrival of the particle in the calorimeter.

To account for a constant bias in the CFD estimator arising from the difference between the front pulse time of arrival and the true time, the mean residual obtained on the training sample was subtracted from all test results. This correction serves purely to remove a fixed offset, which would also be calibrated for in a real detector implementation. The constant offset was calculated on the training data for both the original and reconstructed pulses.

Figure 4 shows the distributions of CFD timing residuals between reconstructed and simulated arrival times. The left panel compares the residuals obtained from the original 32-sample pulses and from the autoencoder-reconstructed pulses using identical CFD parameters. After applying the constant-bias calibration (mean subtraction estimated on the training set), both distributions are centred roughly around zero, as expected. The key comparison of interest is the width of the distributions. The reconstructed pulses exhibit a substantially narrower residual distribution than the original 32-sample pulses, indicating an improvement in timing precision of about a factor of two. Additionally, the right panel presents the ratio of absolute residuals for the reconstructed pulses over the absolute residuals of the original pulse. This quantifies the event-by-event performance gain, which is better than two (i.e. a ratio less than 0.5) for approximately half of the events. The units for the standard deviation shown in Figure 4 (left) are expressed in sampling intervals. Assuming the upper end of the expected sampling period for the readout—approximately 200 ps \S —this corresponds to a standard deviation of about 30 ps for the reconstructed pulses and 62 ps for the original pulses. However, it should be emphasized that the simulation used in this study does not incorporate the final version of the digitizer, and therefore, the approximate “downsampling” performed manually may not fully represent the characteristics of the final digitized output and, therefore, the final expected timing-resolution.

Overall, however, the results confirm that the autoencoder effectively denoises and restores the temporal structure of the pulses, and that is smoothing effect actually leads to a far more accurate and stable CFD-based timestamp reconstruction.

The histogram in Fig. 5 quantifies how accurately the reconstructed pulses reproduce the temporal characteristics of the original waveforms by comparing the deviation of their 10–90 % rise times from the “true” rise-time, which is taken as that found on the original 1024-sample pulses. Similarly to the CFD residuals, the mean bias in the rise-time difference due to downsampling from 1024 to 32 samples

\S https://indico.cern.ch/event/1502285/contributions/6554431/attachments/3081316/5592641/SPIDER_oral_TWEPP2025.pdf

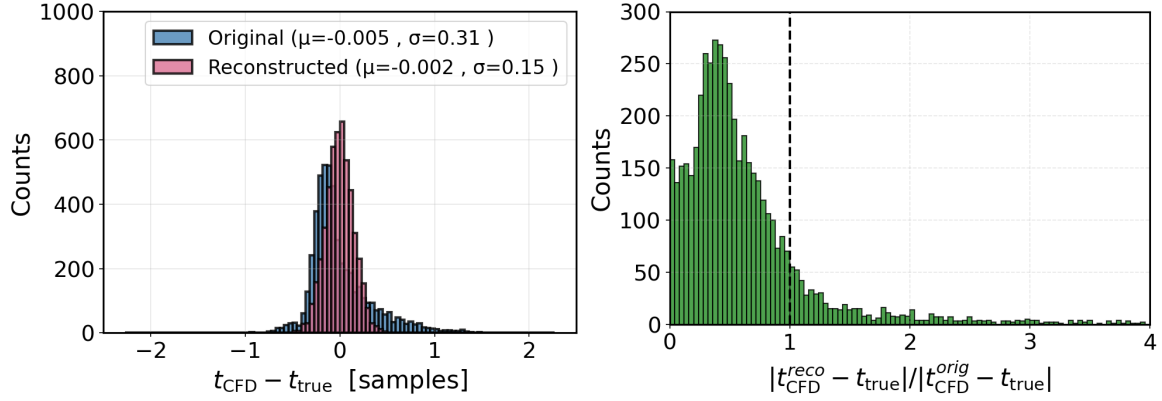


Figure 4. Residual distributions between CFD-reconstructed timestamps and true simulation times for original and autoencoder-reconstructed pulses (left), and the ratio of their absolute values (right). Reconstruction systematically reduces the timing residual for approximately half of the events.

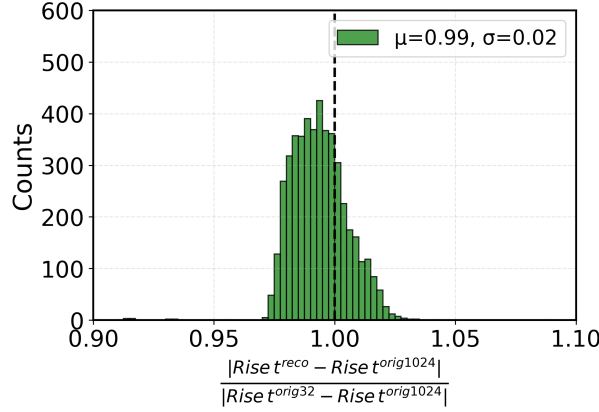


Figure 5. Histogram of the ratio of absolute differences in 10–90 % rise time: (reconstructed vs. 32-sample original) relative to (32-sample original vs. 1024-sample original).

was subtracted separately for the original and reconstructed pulses using the training dataset before ratio evaluation. This ensures that the comparison focuses on the relative reconstruction precision rather than on the systematic offset introduced by coarser sampling. The autoencoder successfully restores fine temporal features lost during the 32-sample discretisation, achieving rise-time consistency with the full-resolution (1024-sample) reference within a few percent and again showing a modest increase in performance compared to the original 32-sample pulses.

3.7. Timestamp Regression

To validate our approach, we investigated whether a model with the same number of layers but trained to directly regress the timestamp from the 32-sample pulse (i.e. 32 → 1) could outperform the autoencoder-based reconstruction followed by the CFD evaluation. In this setup, the network contained no activation function in the output,

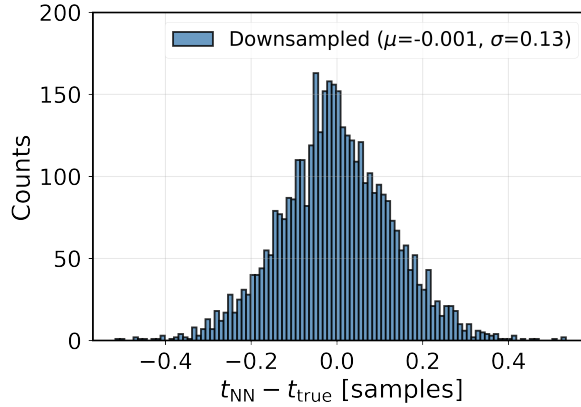


Figure 6. Timestamp–residual distributions for the timestamps predicted using linear regression. The panel shows the histogram of $\Delta t = \hat{t} - t_{\text{true}}$; the legend reports the mean μ and standard deviation σ . All values are in units of samples.

making it equivalent to a linear regressor. The model was trained jointly on both front and back pulses, in the same way as the baseline autoencoder in this paper, to ensure a fair comparison. However, better performance is achievable if the model is trained separately. The residuals ($t_{\text{pred}} - t_{\text{true}}$), shown in Fig. 6, were then analyzed.

These results indicate that the direct timestamp regression achieves a modest improvement over the default model ($\sigma = 0.13$ vs $\sigma = 0.15$). However the 32–2 autoencoder also provides a compact, denoised pulse representation that can support other reconstruction tasks and aid in identifying anomalous signals such as pile-up–induced double peaks. In either case, since this study demonstrates that a 32–2 model can be implemented within the available processing logic, reducing it to a 32–1 model would be straightforward. Future work should determine the level of compression that ultimately provides the optimal balance between performance and efficiency.

4. Hardware-Aware Quantization for Efficient FPGA Inference

4.1. Quantization and Impact Analysis

To prepare the autoencoder for an efficient hardware implementation, the model’s inputs, activations, and weights were converted to fixed-point data types. A mixed-precision scheme was adopted to optimize hardware resource usage while preserving physics performance. The final configuration uses a 16-bit fixed-point representation with 6 integer bits, denoted as $< 16, 6 >$, for the model’s inputs and layer activations. For the computational core of the model, the dense layer’s weights and biases were quantized more aggressively to a 10-bit fixed-point representation with 4 integer bits, $< 10, 4 >$.

This choice is supported by the quantization scan shown in Figure 7. The reconstruction error (MSE) improves significantly as precision increases from 2 to 8 bits and begins to plateau around 10 bits. Additionally, Figure 7 shows the

histograms of MSE values on the test sample for the full-precision and for the quantized models. This confirms that using a 10-bit precision for the weights provides a reconstruction performance nearly identical to that of a full-precision model, justifying the aggressive quantization. This hardware-aware compression drastically reduces the model’s complexity with a negligible impact on its ability to reconstruct the original pulse shapes.

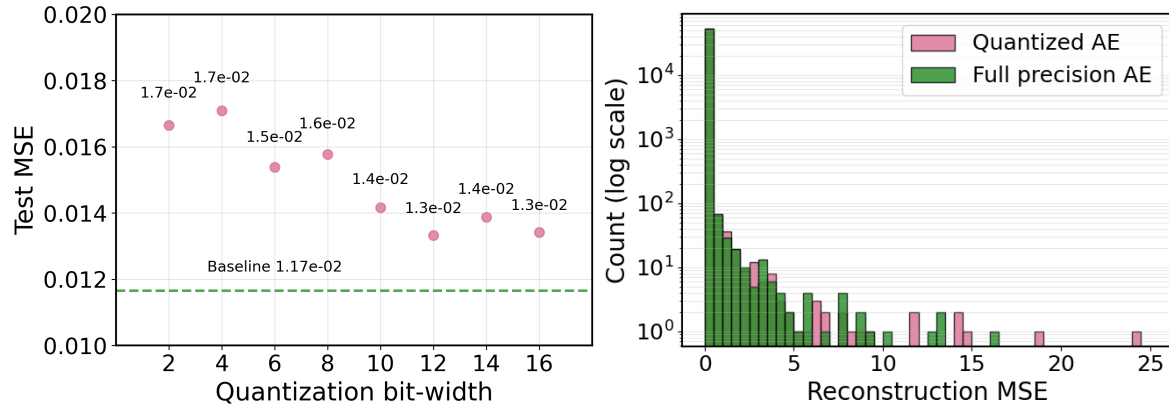


Figure 7. The impact of quantization on the autoencoder’s reconstruction performance (left). The average Mean Squared Error (MSE) is evaluated on the test dataset for different fixed-point bit widths. The green dashed line shows the MSE for non-quantized model. On the right is the distribution of the test MSE for the full precision model vs quantized to 10 bits.

5. Enabling ML on Radiation-Hard FPGAs: A New `hls4ml` Backend and Synthesis Results

With an optimized model, the final step is to translate it into firmware for the target FPGA. This required developing new community infrastructure and synthesizing the design to verify its performance against the strict operational constraints of the front-end electronics.

5.1. A New Backend for `hls4ml`: Targeting Microchip SmartHLS

The core of our engineering contribution is the development of a new backend for `hls4ml` that targets the Microchip SmartHLS compiler. This effort effectively bridges the gap between the HEP ML ecosystem and the target hardware platform. The development process involved a systematic translation of the entire compilation flow. To ensure correctness, the development began with a manual C++ implementation to establish a functional baseline for the SmartHLS compiler. While this manual implementation was sufficient for the autoencoder in this study, the primary goal was to create a reusable, automated path for the community. The development of the backend required significant modifications to both the C++ templates and the Python code-generation

framework. Key steps included: adapting and optimizing the baseline C++ algorithms to use SmartHLS-native libraries and pragmas; expanding the `hls4ml` Python data type system to map quantized tensors to the new data types used by SmartHLS (e.g., `hls::ap_fixpt`); writing a new code-generation engine tailored to SmartHLS intricacies; and creating the build scripts to integrate the new compiler into the `hls4ml` workflow. A rigorous validation process was critical to the development, using C-simulations to confirm that the output of the new backend was bit-for-bit identical to that from established `hls4ml` flows. To ensure a robust hardware verification path, and in coordination with the vendor’s technical team, a streaming interface using FIFO buffers was implemented for the top-level module. This design pattern was adopted on their advice to ensure maximum compatibility and to streamline the Software/Hardware co-simulation flow with the current version of the SmartHLS toolchain.

The culmination of this effort was the integration of these changes into a new, fully-fledged `hls4ml` backend that smoothly integrates into the existing Python API. This new backend, which will be made publicly available, democratizes access to this class of radiation-hard FPGAs for the scientific community.

5.2. Synthesis and Performance on PolarFire FPGA

The quantized model was then processed by our new `hls4ml`-SmartHLS backend to generate HDL code. An important aspect of the hardware implementation relates to how the quantized operations are mapped to the FPGA fabric. The aggressive quantization of the model’s weights to a 10-bit fixed-point representation means that the resulting multiplications are implemented efficiently using the general-purpose 4-input LUTs (Look-Up Tables) rather than the dedicated 18x18 Math Blocks. This behavior, which is consistent with other HLS tools, makes the design highly resource-efficient and underscores the importance of the hardware-aware quantization detailed in Section 4. By tailoring the arithmetic precision, the model avoids relying on specialized DSP resources, which are a limited resource on the FPGA.

This code was subsequently synthesized, placed, and routed considering a target Microchip PolarFire MPF100T-FCVG484I device using the Microchip Libero software to obtain the final implementation results. The post-synthesis timing analysis confirms that the design significantly exceeds the requirements, achieving a maximum frequency (Fmax) of 234 MHz, well above the target of 160 MHz.

The post-synthesis resource utilization and performance metrics are summarized in Table 1. The implementation is remarkably efficient, achieving an inference latency of just 25 ns (4 clock cycles at 160 MHz). With an initiation interval (II) of 4 clock cycles, the accelerator can process new data every 25 ns, comfortably meeting the 40 MHz data rate requirement of the LHCb front-end. The resource footprint is minimal, consuming just 3.1% of the FPGA’s logic (LUTs) and 0.3% of its dedicated math blocks. This confirms the solution is not only fast enough for real-time processing but also lightweight enough to be easily integrated alongside other critical logic on the front-end electronics.

Table 1. Post-synthesis resource utilization per channel and performance for the autoencoder model on a Microchip PolarFire MPF100T-FCVG484I FPGA.

Parameter	Value
Target Clock Frequency	160 MHz (6.25 ns period)
Latency	4 clock cycles (25 ns)
Initiation Interval (II)	4 clock cycles
Resource	Used / Available (Utilization %)
4-input Look-Up Tables	3,385 / 108,600 (3.12%)
D-Flip-Flop	1,545 / 108,600 (1.42%)
Math Blocks (18x18)	1 / 336 (0.30%)
LSRAM	0 / 352 (0%)
uSRAM	0 / 1,008 (0%)

6. Discussion

The results presented in the previous sections demonstrate a complete, end-to-end solution for ML-based on-detector data compression using FPGAs, from algorithm conception to successful hardware implementation, although it should be stressed the synthesis results are based on Software/Hardware co-simulation. Here, we discuss the implications of these findings, both for the immediate LHCb Upgrade II use case and for the wider community seeking to deploy machine learning in harsh environments.

6.1. Feasibility for the LHCb Upgrade II Use Case

A primary goal of this work was to investigate viable solutions for the PicoCal data bandwidth challenge. It was demonstrated that compressing the signal to two 10-bit numbers preserves the full pulse shape. The rising time and peak amplitude could still be extracted from the compressed pulse, and applying a traditional CFD algorithm to the compressed waveform even yielded improved timestamp resolution compared to the original pulse, due to the smoothing of noise effects. Note that ML-alternatives to the CFD algorithm should be the subject of future work.

The hardware implementation results confirm that our approach is not only viable but highly effective. The autoencoder model is extremely lightweight, consuming a negligible fraction of the PolarFire FPGA’s resources, as shown in Table 1. This is a critical success factor, as it ensures that the data compression block can be easily integrated onto the front-end electronics without interfering with other necessary functionalities.

Furthermore, the achieved latency of 25 ns and throughput equivalent to the 40 MHz bunch crossing rate meet the demanding real-time requirements of the LHCb trigger and data acquisition system. The successful synthesis proves that a sophisticated ML model can perform a complex task like pulse shape compression well within the allotted time budget. This provides a strong proof-of-principle for the consideration of this

implementation by the LHCb collaboration for its future upgrade [4].

A crucial aspect of this feasibility study is the scalability of the solution to meet the system’s architectural requirements. The resource utilization reported in Table 1 corresponds to a single autoencoder instance for one calorimeter channel. As noted, the baseline design for the PicoCal front-end board assumes that each FPGA will process 8 channels. Assuming a parallel implementation where each channel requires a dedicated encoder, the total resource footprint would scale linearly. This would project a total utilization of approximately 25% of the FPGA’s 4-input LUTs ($8 \times 3.10\%$) and 2.4% of its Math Blocks ($8 \times 0.30\%$). This projected usage remains modest and falls comfortably within preliminary resource budgets discussed for this processing task. It leaves a substantial fraction of the FPGA’s resources available for other critical functionalities, such as data aggregation and control logic. This analysis confirms that the proposed solution is not only performant for a single channel but also highly scalable to the multi-channel requirements of the final system.

6.2. The Broader Impact of the `hls4ml-SmartHLS` Backend

Perhaps the most significant and lasting contribution of this work is the development of the new `hls4ml` backend for Microchip’s SmartHLS compiler. By creating this piece of open-source infrastructure, we have removed the primary barrier to entry for using radiation-hard PolarFire FPGAs for machine learning inference. This tool makes a new class of radiation-hard devices accessible to the entire high-energy physics community and beyond.

This automated approach provides a significant advantage over a one-off, manual implementation. While the specific autoencoder in this study could have been realized with a manual HLS design, such a solution would lack scalability and reusability. The `hls4ml` backend, in contrast, empowers the community to rapidly prototype and deploy a wide variety of models without requiring bespoke HLS development for each. This automation was also key to our own design process, enabling the systematic hardware-aware quantization scan presented in Section 4, a crucial optimization step that would have been impractical within a manual design flow.

Experiments at the HL-LHC, future colliders, or in space-based applications can now follow a standard, streamlined workflow to deploy ML models on these robust FPGAs. This accelerates the development cycle and empowers domain experts who are not necessarily FPGA design specialists to implement powerful, on-detector ML solutions.

It is important to note that the backend, in its current state, supports the specific layers required for this work, namely dense layers and ReLU activations. The immediate plan is to maintain this functionality, providing a robust and stable tool for similar applications. Future development will be driven by community needs, with plans to expand the library of supported layers as new use cases and requirements emerge.

The backend is publicly available and is scheduled for integration into the main

library as part of the `hls4ml` v1.3.0 release.

6.3. Radiation Hardness: A Holistic View

A key consideration for any electronics deployed in the LHC tunnel is tolerance to radiation-induced errors [2]. Our hardware implementation reveals a powerful synergy between our lightweight algorithm and the inherent robustness of the target hardware. The autoencoder model is so resource-efficient (see Table 1) that its core logic can be physically placed in a radiation-protected region of the FPGA. This leverages the SEU-immune nature of the flash-based configuration memory in the PolarFire® FPGA family and benefits from the reduced radiation exposure of this region. Flash-based FPGAs, such as the Microchip PolarFire family used in this work, store their configuration in nonvolatile memory that is inherently immune to configuration SEUs, removing the need for configuration scrubbing or configuration-level TMR required in SRAM-based FPGAs. However, unlike radiation-hardened or space-qualified components, the user logic fabric is not natively protected against SEUs affecting the data path. Registers, state machines, logic elements, and embedded memories remain susceptible to radiation-induced upsets. Therefore, mitigation techniques like TMR or correction techniques may still be required to protect critical functional paths and maintain reliable operation.

In applications where a model is too large for such physical protection, algorithmic mitigation becomes essential. A common approach is a full TMR of the model, which algorithmically strengthens the design against SEUs at the cost of increased resource consumption. In cases where the resource overhead of full TMR is prohibitive, more granular techniques can be applied. For instance, selective persistence approaches, like those enabled by the FKeras framework [18], can identify the most critical fraction of a model’s parameters that require triplication, offering a balance between robustness and resource usage. Alternatively, one could follow fault-aware, quantization-aware training methodologies. These advanced techniques create models that are, by construction, both performant and inherently resilient to faults, making them radiation-hard with minimal redundancy [19]. These algorithmic mitigation strategies can further expand the radiation protection offered by the approach described in this paper should a model’s resource utilization exceed the capacity of the FPGA’s inherently protected logic.

6.4. Future Directions: Quantifying Physics Performance Gains

The results presented in this paper provide a strong proof-of-principle for the on-detector compression of calorimeter signals. The ultimate validation, however, will be to quantitatively measure the performance gain achieved by using the compressed information in downstream physics tasks.

A key future study will be to integrate the two-dimensional latent space variables into the clustering algorithms used for reconstructing neutral particles. It is expected that the rich pulse shape information preserved in the latent space—which goes far beyond a single timestamp variable—will be crucial for correctly associating energy

depositions with their parent particle clusters. This is particularly important for mitigating the effects of increased pile-up, where the ability to disentangle overlapping signals directly impacts the final energy resolution of the measurement.

Such a quantitative analysis was beyond the scope of this design study, primarily because the official clustering algorithms for the LHCb Upgrade II, which include timing information, are not yet finalized. The development of these future reconstruction algorithms, which will be designed specifically to exploit precision timing information, is a prerequisite for measuring the full physics impact of the compression strategy demonstrated in this work.

7. Conclusion

The increasing data rates and harsh radiation environments of future high-energy physics experiments necessitate the development of novel, on-detector machine learning solutions using FPGAs. This paper presents the first end-to-end demonstration of such a system, using the specific data compression challenge of the LHCb Upgrade II PicoCal calorimeter as a testing-ground.

We have successfully delivered on a three-fold contribution. First, we developed a lightweight autoencoder that effectively compresses the 32-sample detector pulse shapes into a compact, two-dimensional latent space while preserving the critical information needed for physics reconstruction. Second, we performed a hardware-aware optimization of the model, using quantization to create a highly efficient fixed-point representation with a negligible loss in physics performance. Third, and most significantly, we developed a new backend for the `hls4ml` library, enabling for the first time the automatic deployment of ML models on radiation-hard Microchip PolarFire FPGAs via the SmartHLS compiler.

Our synthesis results for the target PolarFire FPGA confirm that the implementation is highly efficient. It achieves an inference latency of just 25 ns and a throughput of 40 MHz, meeting the stringent requirements of the LHCb front-end system. The design utilizes a minimal fraction of the device’s resources ($\approx 25\text{--}30\%$ of logic and less than 10% of DSPs for 8 channels). This efficiency allows the model to reside entirely within the FPGA’s inherently radiation-hard logic fabric, providing a robust solution for this use case without the need for complex mitigation schemes.

This work transforms a challenging data compression problem into a demonstrated reality. The development of the open-source `hls4ml`-SmartHLS backend, in particular, provides a lasting contribution to the scientific community, paving the way for a new wave of intelligent, radiation-hard detector systems at the frontiers of science. Future work will focus on expanding the backend’s layer support to broaden its applicability for the community.

Acknowledgements

The authors would like to thank the LHCb collaboration for providing the context and resources for this design study. We especially thank the Upgrade II team and the Syracuse LHCb group for providing the simulated samples used to train and evaluate the performance of the autoencoder. We are also grateful for the fruitful discussions with our colleagues within the LHCb data processing team that helped improve this work, including Felipe Souza de Almeida, Nuria Valls Canudas, Christophe Beigbeder, Zulal Kiraz, Christina Agapopoulou, Marina Artuso, Matthew Rudolph, Lauren Mackey, Patrick Robbe and Philipp Roloff. We wish to express our gratitude to the development and support team of Microchip’s SmartHLS for their valuable assistance in enhancing the compatibility of the `hls4ml` library with their framework.

Code Availability

The `hls4ml` backend developed for this work is publicly available on GitHub at <https://github.com/fastmachinelearning/hls4ml/pull/1240>.

References

- [1] I. Zurbano Fernandez et al. High-Luminosity Large Hadron Collider (HL-LHC): Technical design report. 10/2020, 12 2020.
- [2] Ian Dawson, F Faccio, M Moll, and A Weidberg. Radiation effects in the lhc experiments: Impact on detector performance and operation. *CERN Yellow Reports: Monographs, Geneva: CERN*, pages 87–122, 2021.
- [3] Roel Aaij et al. Physics case for an LHCb Upgrade II - Opportunities in flavour physics, and beyond, in the HL-LHC era. 8 2018.
- [4] Framework TDR for the LHCb Upgrade II: Opportunities in flavour physics, and beyond, in the HL-LHC era. 2021.
- [5] Ludovic Alvado, Nicolas Arveuf, Edouard Bechettoille, Guillaume Blanchard, Dominique Breton, Baptiste Joly, Laurent Leterrier, Jihane Maalmi, Samuel Manen, Hervé Mathez, Christophe Sylvia, Philippe Vallerand, and Richard Vandaele. Spider, a waveform digitizer asic for picosecond timing in lhcb picocal, 2025.
- [6] Javier Duarte et al. Fast inference of deep neural networks in FPGAs for particle physics. *JINST*, 13(07):P07027, 2018.
- [7] Farah Fahim, Benjamin Hawks, Christian Herwig, James Hirschauer, Sergo Jindariani, Nhan Tran, Luca P Carloni, Giuseppe Di Guglielmo, Philip Harris, Jeffrey Krupa, et al. hls4ml: An open-source codesign workflow to empower scientific low-power machine learning devices. *arXiv preprint arXiv:2103.05579*, 2021.

- [8] Alexander Radovic, Mike Williams, David Rousseau, Michael Kagan, Daniele Bonacorsi, Alexander Himmel, Adam Aurisano, Kazuhiro Terao, and Taritree Wongjirad. Machine learning at the energy and intensity frontiers of particle physics. *Nature*, 560(7716):41–48, 2018.
- [9] Marco Farina, Yuichiro Nakai, and David Shih. Searching for new physics with deep autoencoders. *Phys. Rev. D*, 101:075021, Apr 2020.
- [10] Buhmann, Erik, Diefenbacher, Sascha, Eren, Engin, Gaede, Frank, Kasieczka, Gregor, Korol, Anatolii, and Krüger, Katja. Decoding photons: Physics in the latent space of a bib-ae generative network. *EPJ Web Conf.*, 251:03003, 2021.
- [11] F Lima Kastensmidt, Luca Sterpone, Luigi Carro, and M Sonza Reorda. On the optimal design of triple modular redundancy logic for sram-based fpgas. In *Design, Automation and Test in Europe*, pages 1290–1295. IEEE, 2005.
- [12] Framework TDR for the LHCb Upgrade II. Technical report, CERN, Geneva, 2021.
- [13] S. Agostinelli et al. Geant4 simulation toolkit. *Nuclear Instruments and Methods in Physics Research Section A: Accelerators, Spectrometers, Detectors and Associated Equipment*, 506(3):250–303, 2003.
- [14] Aleksandar Bordelius. The lhcb picocal. *Nuclear Instruments and Methods in Physics Research Section A: Accelerators, Spectrometers, Detectors and Associated Equipment*, 1079:170608, 2025.
- [15] Martín Abadi et al. TensorFlow: Large-scale machine learning on heterogeneous systems, 2015. Software available from tensorflow.org.
- [16] François Chollet et al. Keras. <https://keras.io>, 2015.
- [17] D.A. Gedcke and W.J. McDonald. A constant fraction of pulse height trigger for optimum time resolution. *Nuclear Instruments and Methods*, 55:377–380, 1967.
- [18] Olivia Weng, Andres Meza, Quinlan Bock, Benjamin Hawks, Javier Campos, Nhan Tran, Javier Mauricio Duarte, and Ryan Kastner. Fkeras: A sensitivity analysis tool for edge neural networks. *ACM J. Auton. Transport. Syst.*, 1(3), July 2024.
- [19] Muhammad Abdullah Hanif and Muhammad Shafique. Faq: Mitigating the impact of faults in the weight memory of dnn accelerators through fault-aware quantization. *arXiv e-prints*, pages arXiv–2305, 2023.